Direct, high resolution, four-dimensional measurements of the fine scale structure of Sc ≫ 1 molecular mixing in turbulent flows

Werner J. A. Dahm, Kenneth B. Southerland, and Kenneth A. Buch
Department of Aerospace Engineering, The University of Michigan, Ann Arbor, Michigan 48109-2140

Results from highly resolved, four-dimensional measurements of the fine structure of the fully space- and time-varying Sc ≫ 1 conserved scalar field and the associated scalar energy dissipation rate field in a turbulent flow are presented. The resolution achieved in all three spatial dimensions and in time reaches down to the local strain-limited molecular diffusion scale in the flow, allowing all three components of the instantaneous scalar gradient vector field $\nabla\zeta(\mathbf{x},t)$ and their time evolution at every point in the data space to be directly evaluated. Results are presented in the form of fine structure maps of the instantaneous dissipation field $\log_e \nabla\zeta\cdot\nabla\zeta(\mathbf{x},t)$ in several spatially adjacent data planes within an individual three-dimensional spatial data volume, as well as in several temporally successive data planes from a sequence of such three-dimensional data volumes. The degree of anisotopy in the underlying scalar gradient field is characterized in terms of the joint distribution $\beta(\vartheta,\varphi)$ of spherical orientation angles. The probability density of true scalar energy dissipation rates is presented and compared with the distributions that would result from lower-dimensional measurements of the scalar gradient vector. From this the "spottiness" of the scalar dissipation field is directly quantified by determining the true fraction of the total dissipation that occurs in any given volume fraction of the flow.

I. INTRODUCTION

Molecular mixing in turbulent flows plays a central role in an enormous range of practical problems. Many such problems can be formulated, either directly or in certain limiting cases, in terms of the mixing of a dynamically passive conserved scalar quantity. By this we refer to any scalar quantity that is advected with the fluid and diffuses relative to the fluid, but which is neither created nor destroyed within the flow and which does not directly affect the flow field. Examples include the mixing of temperature, salinity, or organic matter within the oceans, the dispersal of pollutants within the atmosphere, the mixing of two different inert gaseous streams, or even the evolution of the atomic mixture fraction in reacting flows. Sometimes the diffusivity D of the quantity being mixed is comparable to the vorticity diffusivity ν of the fluid; in other words the Schmidt number $Sc \equiv (\nu/D)$ is approximately unity. However, in many other cases the diffusivity of the scalar is much smaller than that of the vorticity, so that Sc ≫ 1. Examples in this latter class include the mixing of fine particulates such as soot or droplets in the atmosphere, the mixing and reaction of aqueous acid–base solutions, or the mixing of various constituents in a wide range of chemical, pharmaceutical, and industrial processes. In many problems of this type, and especially those in which some sort of reaction or phase change is involved, it is processes occurring at the fine structure level of the scalar field that can be crucially important in determining the outcome of the mixing. The fine structure of scalar mixing in turbulent flows is, however, a subject of inherently much wider interest, since it indirectly contains information about the underlying fine scale vortical structure of the turbulent

flow itself. For these reasons, an understanding of the fine structure of conserved scalar mixing in turbulent flows has been a topic of longstanding interest in fluid mechanics.

It was recognized some time after the introduction of Kolmogorov's[1] universal similarity hypothesis that some aspects of this theory also applied to the fine structure of dynamically passive scalar fields being mixed in high Reynolds number turbulent flows. The subsequent modifications to Kolmogorov's original hypothesis of a homogeneous statistical distribution of the dissipation, introduced to account for the spatial "spottiness" of the vorticity and kinetic energy dissipation, have their parallels in the scalar field fine structure. In particular, Batchelor[2] recognized that, when the scalar diffusivity D is significantly smaller than the vorticity diffusivity ν, the essentially uniform strain rate ϵ over regions in the flow much smaller than the finest vortical length scale λ_ν provides a mechanism for sustaining scalar gradients over length scales $\lambda_D \ll \lambda_\nu$. The limiting scale λ_D in the scalar field then results from a competition between the compression due to this strain field and diffusion of the scalar, giving $\lambda_D \sim (D/\epsilon)^{1/2}$. This picture of a strain–diffusion balance setting the finest length scales in the mixing of a scalar field is of course precisely the mechanism in Burgers'[3] and Townsend's[4] solutions of sheets and lines as the canonical fine structure elements for the vorticity and kinetic energy dissipation fields in turbulent flows. [A discussion of these strain-limited solutions for vortex "sheets" and "lines" in steady strain fields is given by Sherman;[5] see pp. 155–156 and pp. 564–567; see also Batchelor[6] pp. 271–273. The extension to time-varying strain fields is given by Carrier et al.;[7] see their Eqs. (4.1)–(4.4).] Indeed, in both these line and sheet solutions, the vorticity is merely a dynamically

passive scalar quantity being advected by the flow and diffusing relative to the flow. As a consequence, these line and sheet solutions are also candidates for the underlying canonical fine structure elements of passive scalar fields being mixed in turbulent flows. It is interesting to note that such a view of lamellar microstructure can also be seen in recent experiments on mixing in low Reynolds number chaotic flows (e.g., Ottino;[8,9] Ottino et al.[10]), and have been developed into a range of models for predicting various aspects of mixing and chemical reactions in fluid flows (e.g., Ottino et al,[10] Ottino;[11-13] Bourne[14]).

Until recently, however, direct experimental measurements capable of discerning the scalar field fine structure in turbulent flows have not been possible. Dahm and Buch[15-17] introduced highly resolved, three-dimensional spatiotemporal measurements of Sc $\gg$ 1 conserved scalar mixing from which they concluded that the sheet-like solution referred to above forms the sole underlying canonical element of the scalar field fine structure. However, their experiments involved measurements in only two of the three spatial dimensions and thus, on the one hand, inherently underestimated the mixing rate when the scalar gradient had a strong component in the third spatial direction, and on the other hand, required the assumption of isotropy in the scalar field to determine certain quantitative characteristics of the mixing. More recently, Dahm et al.[18] developed a technique for obtaining highly resolved four-dimensional measurements of the space- and time-varying conserved scalar field in a turbulent flow, from which the true fine structure of the mixing process can be determined. In this paper, we present measurements obtained with this technique and use them to analyze several aspects of the underlying fine structure of Sc $\gg$ 1 molecular mixing in turbulent flows.

A. Formulation

In the mixing of any generic conserved scalar quantity ζ, the conserved scalar field $\zeta(\mathbf{x},t)$ satisfies the advection–diffusion equation

$$\left(\frac{\partial}{\partial t} + \mathbf{u}\cdot\nabla - \frac{1}{\text{Re Sc}}\nabla^2\right)\zeta(\mathbf{x},t) = 0. \qquad (1)$$

Here all variables have been made nondimensional by normalization with suitable reference length and velocity scales, l^* and u^*, and reference scalar value ζ^*. Equation (1) involves only the product Re Sc of the Reynolds number $\text{Re} \equiv (u^*l^*/\nu)$ and the Schmidt number $\text{Sc} \equiv (\nu/D)$, where ν and D are the vorticity and scalar diffusivities, respectively. However, the transport equations for $\mathbf{u}(\mathbf{x},t)$ introduce the Reynolds number explicitly as

$$\nabla\cdot\mathbf{u}(\mathbf{x},t) = 0, \qquad (2a)$$

$$\left(\frac{\partial}{\partial t} + \mathbf{u}\cdot\nabla - \frac{1}{\text{Re}}\nabla^2\right)\mathbf{u}(\mathbf{x},t) = -\frac{\nabla p}{\rho}, \qquad (2b)$$

and as a consequence the scalar field structure can in general depend on both Re and Sc. From (1), the associated scalar energy per unit mass $\frac{1}{2}\zeta^2(\mathbf{x},t)$, defined analogous to the kinetic energy per unit mass $\frac{1}{2}u^2(\mathbf{x},t)$, where $u \equiv |\mathbf{u}|$, follows the exact transport equation

$$\left(\frac{\partial}{\partial t} + \mathbf{u}\cdot\nabla - \frac{1}{\text{Re Sc}}\nabla^2\right)\frac{1}{2}\zeta^2(\mathbf{x},t) = -\frac{1}{\text{Re Sc}}\nabla\zeta\cdot\nabla\zeta(\mathbf{x},t), \qquad (3)$$

where the same conservative advection–diffusion operator appears on the left-hand side, and where on the right-hand side the term $(\text{Re Sc})^{-1}\nabla\zeta\cdot\nabla\zeta(\mathbf{x},t)$ gives the local instantaneous rate of scalar energy dissipation per unit mass, namely the rate at which nonuniformities in the scalar energy field are being reduced by molecular diffusion in the flow. In this context, the scalar dissipation is often adopted as a meaningful quantification for the local instantaneous rate of molecular mixing in the flow. Alternately, the scalar gradient magnitude $|\nabla\zeta(\mathbf{x},t)|$ is also sometimes used to define the mixing rate. We note that in terms of the scaled logarithm of the mixing rate, these two definitions become identical.

The concepts of scalar energy and its dissipation rate play a central role in many approaches for understanding and modeling molecular mixing in turbulent flows, including those where chemical reactions are present. However, direct measurements of these quantities have been difficult to obtain. This has been principally due to two obstacles. First, determination of the true scalar gradient field $\nabla\zeta(\mathbf{x},t)$ and the associated scalar dissipation rate field $\nabla\zeta\cdot\nabla\zeta(\mathbf{x},t)$ requires measurement of the conserved scalar field $\zeta(\mathbf{x},t)$ in all three spatial dimensions. Second, since the dissipation rate is obtained by differentiation of the measured conserved scalar field, the spatial and temporal resolution of the original scalar measurements must be high enough to accurately resolve the finest length and time scales on which gradients in the scalar field are present in the flow. Beyond these requirements, the signal quality of the original scalar field measurements must also be high enough to permit accurate differentiation to determine the scalar gradient field.

B. Previous work

A number of different approaches used in recent years in attempts to obtain accurate measurements of conserved scalar fields in turbulent flows are summarized in Ref. 18. Almost all of these have made use of various planar laser imaging techniques; a good review of many of these is given by Hanson.[19] Of relevance to the present work, Yip and Long[20] have attempted to extend their measurements[21,22] based on two-dimensional planar laser imaging to yield three-dimensional scalar gradient information by imaging from two parallel and closely spaced laser sheets. However, both the sheet spacing and the pixel separation were significantly larger than the local molecular diffusion scale in the flow. Following a somewhat different approach, Yip and co-workers[23,24] have swept a laser sheet at very high speed through a turbulent flow, in conjunction with very high speed data acquisition over a short duration, to obtain measurements in up to 16 closely spaced parallel planes. However, in these measurements also, as well as more recent ones by Prasad and Sreenivasan,[25] the resolution was sufficient to yield information only at scales significantly coarser than the finest diffusion length scale of the flow.

C. Present work

Here we present results obtained using a laser imaging diagnostic specifically designed for very highly resolved, four-dimensional measurements of the full space- and time-varying conserved scalar field $\zeta(\mathbf{x},t)$ and the associated scalar energy dissipation rate field $\nabla\zeta\cdot\nabla\zeta(\mathbf{x},t)$ in turbulent flows. The resolution achieved is finer than the local strain-limited molecular diffusion scale λ_D, allowing the fine structure of $Sc \gg 1$ molecular mixing in turbulent flows to be directly determined. The measurements presented here were obtained in the self-similar far field of an axisymmetric turbulent jet at an outer-scale Reynolds number $Re_\delta \equiv (u\delta/\nu)$ of 6000, as shown in Fig. 1. Note, however, that the imaged region of the flow was quite small in comparison with the local outer scale δ, and was comparable to the inner scale λ_ν of the flow. In particular, each data plane spanned approximately $\frac{1}{17}$ of the outer scale δ and approximately 1.6 times the inner scale λ_ν in both directions. As a result, if this outer-scale Reynolds number Re_δ is large enough so that on the inner scales $l^* \equiv \lambda_\nu$ and $u^* \equiv (\nu/\lambda_\nu)$, for which $Re \equiv 1$, the velocity $\mathbf{u}$ in Eqs. (1)–(3) has become independent of the outer-scale Reynolds number, then the scalar field fine structure would also be independent of Re_δ and would depend only on the Schmidt number. Furthermore, once the fine structure has become independent of the outer-scale Reynolds number, all memory of the outer scales is lost and the fine structure would then not be particular just to the

turbulent jet, but should apply to mixing in turbulent shear flows in general. In this sense, we believe that many features of the fine structure captured within our four-dimensional data space will to a large degree be generic to large Schmidt number mixing in all high Reynolds number turbulent flows.

II. EXPERIMENTAL TECHNIQUE

The experimental method developed for these measurements is an extension of our earlier work[15-17] in obtaining highly resolved three-dimensional (256^3) spatiotemporal measurements of the conserved scalar concentration field and the resulting scalar energy dissipation rate field in turbulent flows. The technique is briefly described in the following section; additional details are given in Ref. 18.

Our experiments are of mixing in a turbulent shear flow in water. In particular, the measurements are conducted in the self-similar far field of an axisymmetric turbulent jet issuing into an essentially quiescent medium. The mixture fraction is defined here by the concentration of a dynamically passive dilute laser fluorescent dye (disodium fluorescein) carried by one of the fluids, and is a conserved scalar for which the Wilke–Chang method[26] suggests a value for the Schmidt number of 2075. In our experiments, this mixture fraction is measured repeatedly in time throughout a small three-dimensional volume in the flow by imaging the laser-induced fluorescence from dye-containing fluid in the path of a laser beam rapidly swept in a raster fashion through the volume onto a high-speed planar photosensitive array. The measurements are conducted by issuing a jet through a round nozzle into a $0.8 \times 0.8 \times 1.8$ m glass tank filled with water, in which a very small coflow (5.75 cm/min) ensures that there is no recirculation of dyed fluid to contaminate the imaged volume in the flow. For this coflowing velocity, the measurement volume is approximately one coflow momentum diameter downstream of the nozzle, placing it well within the pure jet limit of the flow (e.g., see Biringen[27]).

The successive laser-induced fluorescence data planes can be rapidly acquired into gigabyte sized data sets using very fast computer disk ranks to produce a four-dimensional spatiotemporal data space structured as shown in Fig. 2. Each such measured data space consists of a rapid succession of individual three-dimensional spatial data volumes. Each of these data volumes is itself composed of a sequence of two-dimensional spatial data planes, which in turn each consist of an array of 256×256 individual data points. The spatial separation between adjacent points within each data plane, and between adjacent data planes within each data volume, is smaller than the local strain-limited molecular diffusion length scale λ_D of the scalar field. Similarly, the temporal separation between adjacent data planes within each data volume, and between the same data plane in successive data volumes, is shorter than the local molecular diffusion scale advection time λ_D/u. This resolution, together with the high signal quality attained, allows accurate differentiation of the measured conserved scalar data in all three space dimensions and in time to determine the components of the local instantaneous scalar gradient vector field $\nabla\zeta(\mathbf{x},t)$ at every point in the data space. From this, the true
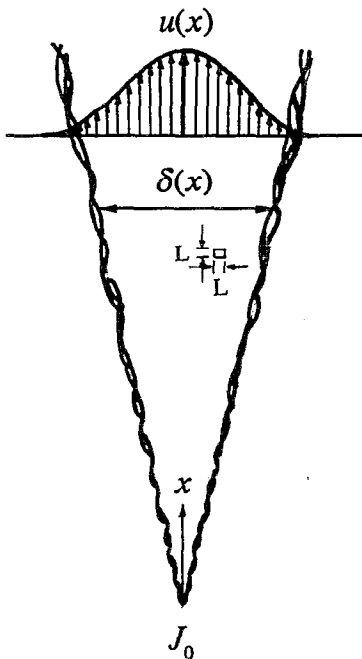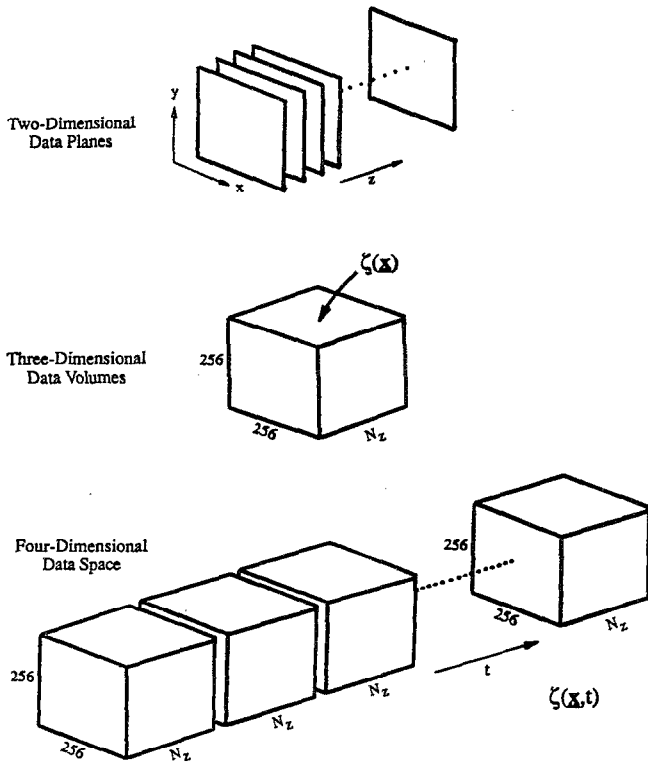
FIG. 1. The scalar field is measured in the self-similar far field of an axisymmetric turbulent jet in water at an outer-scale Reynolds number Re_δ of 6000. The approximate size (L) and location of the imaged region of the flow are indicated. In terms of the local outer scale of the flow, (L/δ) $\approx \frac{1}{17}$, while in terms of the local inner scale, (L/λ_ν) ≈ 1.6. As a result, if Re_δ is large enough so that all memory of the outer scales u and δ is lost on the inner scale of the flow, then the fine structure results obtained from the imaged region will to a large degree be generic to $Sc \gg 1$ mixing in all high Reynolds number turbulent flows.

Two-Dimensional
Data Planes

y

x   z

$\zeta(x)$

Three-Dimensional
Data Volumes

256

256   N_z

Four-Dimensional
Data Space

256

N_z

256   N_z

N_z

256

256   N_z

t

$\zeta(x,t)$

FIG. 2. Structure of the experimentally measured, four-dimensional, spatiotemporal conserved scalar data space $\zeta(x,t)$ as a temporal progression of three-dimensional spatial data volumes, each consisting of a sequence of two-dimensional spatial data planes, each composed of a 256×256 array of data points. The spatial and temporal resolution achieved is sufficient to allow direct differentiation of the conserved scalar data in all three space dimensions and in time, allowing the evolution of the true molecular mixing rate field $\nabla\zeta\cdot\nabla\zeta(x,t)$ to be directly determined.

instantaneous scalar energy dissipation rate field $\nabla\zeta\cdot\nabla\zeta(x,t)$ can be determined.

Key elements of the imaging and data acquisition system assembled for these four-dimensional measurements are shown schematically in Fig. 3. A pair of very low inertia, galvanometric mirror scanners are used to synchronously sweep a collimated laser beam in a raster scan fashion through the desired volume in the flow field. The principal objectives of the scanner drive electronics are to synchronize the beam sweep with the photodiode array timing, so that each data plane corresponds to a single sweep of the beam, and to accommodate the minimum flyback times for the scanners within the period between acquisition of successive data planes. The horizontal and vertical sweep angles used are typically quite small. The resulting laser-induced fluorescence intensity is measured with a 256×256 imaging array, having center-to-center pixel spacings of 40 μm. The array is synchronized to the same clock that drives the scanners, and can be driven at variable pixel rates up to 11 MHz, allowing measurement of successive data planes at a continuous rate in excess of 140 planes per second. The fluorescence data from the array is serially acquired through a programmable digital port interface, digitized to 8-bits digital depth, then routed into a 16 MB high-speed dual-ported data

buffer from which it can be continuously written in real time to a 3.1 GB high-speed parallel transfer disk rank. The overall sustained data throughput rate to the disks, accounting for all line and frame overhead cycles, is up to 9.3 MB/sec. The 3.1 GB disk capacity can accommodate more than 50 000 such measured 256×256 spatial data planes within the four-dimensional data space. Programmable gain and offset on the digital port interface allow the resulting data to span the full 8 bits of digital depth.

To assess the noise content of these measurements, we constructed the histogram of the measured scalar field data over the 256 levels discernible by such 8-bit digital measurements. We then constructed a similar histogram of a set of dark noise data and computed its rms. The noise level in the actual data was verified as being essentially the same as the dark noise by also computing the noise histogram in regions of the data where the nominal signal level was uniform. This was done by constructing templates that covered areas of unmixed ambient fluid in several of the data planes, and then computing the noise histogram within these templates. The resulting noise characteristics were virtually identical to those obtained from the dark fields. Since the mean noise can be removed from the data but the fluctuating noise cannot, the relevant noise figure is a comparison between the rms noise range and the range of values spanned by the actual data. For the same digital port settings, the rms noise measured in this manner is $\pm$ 1 digital signal level out of the 256 levels, while the scalar field data span the entire 256 levels.

A. Spatial and temporal resolution

Since the principal interest in these measurements is in obtaining the scalar dissipation field from the measured conserved scalar field via direct differentiation of the data, the central issue is the spatial and temporal resolution achieved by the measurements. From the measured thickness of the imaged portion of the laser beam, together with the pixel size and the image ratio of the measurements, the volume in the flow ($\Delta x\cdot\Delta y\cdot\Delta z$) imaged onto each pixel can be determined. Furthermore, for the pixel clock rates used, the time Δt between acquisition of successive data planes within each spatial data volume, and the time ΔT between the same data plane in successive data volumes, can also be determined. To assess the resulting relative resolution achieved, these smallest spatial and temporal scales discernible in the data must be compared with the finest local spatial and temporal scales on which gradients in the conserved scalar field can be sustained in the flow. In particular, for local diffusion of vorticity in the presence of a time varying strain rate $\epsilon(t)$, the competing effects of strain and diffusion establish an equilibrium strain-limited vorticity diffusion layer thickness $\lambda_\nu \sim (\nu/\epsilon)^{1/2}$, closely related to the Kolmogorov scale, giving the finest scale on which spatial gradients in the strain rate and vorticity fields can be locally sustained in the flow (e.g., Burgers;[3] Townsend[4]). A similar competition between the effects of strain and molecular diffusion of the conserved scalar establishes a local strain-limited molecular diffusion layer thickness $\lambda_D \sim (D/\epsilon)^{1/2}$, related to the Batchelor scale and giving the smallest scale on which spatial gradients in the conserved scalar field can be sustained by the flow (e.g.,
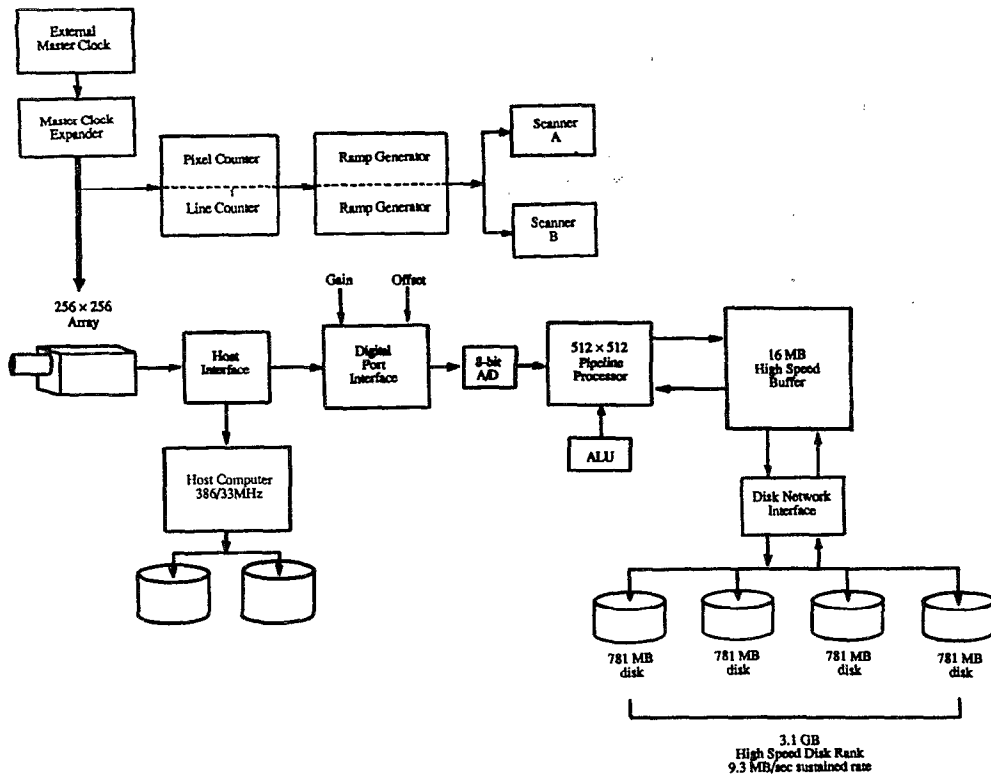
FIG. 3. Key elements of the high-speed variable-rate imaging and data acquisition system assembled for these highly resolved four-dimensional measurements of scalar mixing in turbulent flows. Two low-inertia galvanometric mirror scanners are slaved to the imaging array timing to rapidly sweep the laser beam in a successive raster scan fashion through the scalar field. The data acquisition system can achieve a sustained data throughput rate to the disk rank of up to 9.3 MB/sec for volumes as large as the full 3.1 GB disk capacity.

Carrier et al.;[7] Marble[28]). The ratio of the vorticity and scalar diffusivities, v and D, respectively, establishes the relation between these two scales as $\lambda_D \sim \lambda_v \cdot Sc^{-1/2}$, where $Sc \equiv (v/D)$ is the Schmidt number and where, due to the similarity of the two strain–diffusion equilibrium processes, the proportionality constant should be approximately one. Note that, with the highest strain rates occurring locally in the flow scaling as $\epsilon \sim (u/\delta) \cdot Re_\delta^{1/2}$, with $Re_\delta \equiv (u\delta/v)$ the local outer-scale Reynolds number, the strain-limited diffusion scale in the conserved scalar field is $(\lambda_D/\delta) \sim Sc^{-1/2} Re_\delta^{-3/4}$. Measurements by Dowling[29] and by Dahm and Buch[15-17] give indications that the resulting proportionality constant is roughly 25.

The resolution requirements that Δx, Δy, and Δz must be small compared to λ_D to allow meaningful differentiation in all three space directions within each three-dimensional spatial data volume, and that the time ΔT between the same data plane in successive data volumes must be small in comparison with the fine structure advection time scale (λ_D/u) to allow differentiation in time between data volumes, ultimately place a limit on the highest outer-scale Reynolds numbers at which such highly resolved four-dimensional

measurements are possible. Note that while the resolution Δx and Δy within each spatial data plane can in principle be made very small by simply reducing the image ratio, the resolution Δz is nominally determined by the laser beam thickness. There are clear limitations associated with the Rayleigh range of the laser beam that determine how fine this can be made over the entire extent of the image volume. In general, the resulting minimum laser beam thickness is somewhat larger than the desired spatial separation between successive data planes. However, if the time Δt between successive planes is small enough so that the scalar field is effectively frozen, then the overlap in the measured scalar field between adjacent planes represents a convolution of the true scalar field with the laser beam profile. The measured scalar field was therefore deconvolved with the measured beam profile shape to produce an effective resolution Δz comparable to the spatial separation between adjacent data planes, which is set by the horizontal scanner and can in principle be made quite small. For the laser beam diameter of $380\,\mu m$ and the interplane separation of $220\,\mu m$ in the present measurements, the convolution coefficients are 0.0033–0.170–0.654–0.170–0.0033, so that this overlap effectively

extends only to the next adjacent data plane on either side. Since the elements of the resulting convolution matrix are therefore essentially zero beyond the second off-diagonal elements, we chose to invert only the resulting 5×5 kernel matrix to obtain the deconvolution matrix. (The elements of the resulting deconvolution matrix change only slightly as the size of the kernel matrix increases.) Moreover, the elements of this deconvolution matrix decrease rather rapidly with distance from the main diagonal. For example, in the central row of the deconvolution matrix, the coefficients multiplying each of the two planes immediately adjacent to the centerplane are 28% of the diagonal coefficient, while the coefficients for each of the planes two removed from the diagonal are less than 7% of the center coefficient. As a result, the summation involved in the deconvolution shows that the weighting for each of the planes two removed from the diagonal contribute only about 4% to the total scalar value obtained, and for this reason the deconvolution was truncated to include only the two immediately adjacent planes.

The present measurements were obtained at an axial location 235 jet momentum diameters (1.15 m) downstream of the jet source and a radial location 13 cm off the jet centerline. To estimate the resulting resolution requirements, we note that $\delta(x) \simeq 0.44x$ and $u(x) \simeq 7.2 \, (J/\rho)^{1/2} \cdot x^{-1}$, where J is the jet source momentum flux and ρ is the ambient fluid density. At the outer-scale Reynolds number of 6000 and with the Schmidt number of 2075, these scalings give the local strain-limited molecular diffusion length scale estimate of $\lambda_D \approx 407 \, \mu m$ and the local advection time scale estimate of $(\lambda_D/u) \approx 100$ msec at the location of the measurement volume. With the measurements having an image ratio of 2.89, the in-plane spatial resolution was $\Delta x = \Delta y = 116 \, \mu m$. The measured $(1/e)$ laser beam thickness over the imaged portion of the flow varied from 345 to 390 μm, while the spatial resolution Δz between successive data planes was 220 μm. (Note that these small variations in laser beam diameter were ignored in the deconvolution described above.) These Δx, Δy, and Δz values must be compared with λ_D to assess the relative spatial resolution achieved. In particular note that, for the resulting pixel image volume, $(\Delta x \cdot \Delta y \cdot \Delta z)^{1/3}$ was nearly three times smaller than λ_D, while its maximum dimension (Δz) was nearly two times smaller than λ_D. Similarly, the temporal separation between successive data planes was $\Delta t = 9.0$ msec and the time between successive data volumes was $\Delta T = 45$ msec, both of which are considerably smaller than the estimated local diffusion scale advection time of 100 msec. As a result, the present measurements should be capable of resolving essentially all of the fine scale structure of the local Sc$\gg$1 turbulent mixing process.

III. RESULTS

Analysis of a four-dimensional data space of the type obtained here has many parallels with the analysis of large scale computational data volumes obtained from full numerical simulations of turbulent flows. Both can in principle be analyzed in considerable quantitative detail. However, a significant challenge facing both experiments and numerical simulations of this type is the extraction of insightful interpretations from such a very large amount of data. To this end we rely strongly on quantitative graphical visualization of large subsets of the original data space and numerically processed versions of it to provide guidance into the underlying physical processes contained within the data. Here we choose to focus principally on the topology of the fine structure resulting from Sc$\gg$1 scalar mixing in turbulent flows, and on the structural and associated statistical properties of the corresponding scalar gradient field. Note that all quantities presented have been made nondimensional by the inner-scale reference values $l^* \equiv \lambda_\nu$, $u^* \equiv (\nu/\lambda_\nu)$ and the local mean scalar value $\zeta^* \equiv \zeta_m(x)$.

A. Fine scale structure

Figure 4 shows the 8-bit conserved scalar data in three typical parallel adjacent 256×256 spatial data planes from the same data volume. The 256 color levels denote the local conserved scalar value $\zeta(\mathbf{x},t)$ at each point, with pure blue corresponding to pure ambient fluid ($\zeta = 0$) and increasing uniformly to pure red, corresponding to the highest scalar values in the data ($\zeta = 2.85\zeta_m$). Recall that each data plane shown spans approximately $\frac{1}{17}$ of the local outer scale $\delta(x)$, and approximately 1.6 times the local inner scale $\lambda_\nu(x)$, in each direction. Note that the three spatial data planes are presented in order of increasing z (and therefore increasing time) in the clockwise direction, beginning at the upper left. The relatively small change in the scalar field from one data plane to the next in Fig. 4 is typical of the change between adjacent planes throughout the data space, and reflects the relatively high spatial and temporal resolution of the measurements.

In Fig. 5 we show the true scalar energy dissipation rate field $\log_e \nabla\zeta \cdot \nabla\zeta(\mathbf{x},t)$ obtained by direct differentiation of the data in the three adjacent scalar planes in Fig. 4. Linear central difference approximations have been used to evaluate the three components of the scalar gradient vector field $\nabla\zeta(\mathbf{x},t)$, with no explicit smoothing or filtering of the results. The dissipation field obtained is presented here in logarithmic form because this compression allows a wider range of mixing rates to be displayed. Additionally, we note that in logarithmic form the results are identical to those obtained if the mixing rate is alternately defined as $|\nabla\zeta(\mathbf{x},t)|$. The 256 different color levels now denote increasing values of the mixing rate. The first level, colored black, denotes zero and very low mixing rates, while the remaining levels range uniformly from blue through pure red denoting logarithmically increasing values of the local instantaneous scalar dissipation rate in the flow. For reference, pure red is scaled to the highest 0.1% of the dissipation rates and corresponds to $\nabla\zeta \cdot \nabla\zeta(\mathbf{x},t) = 5647.6(\zeta_m/\lambda_\nu)^2$.

To examine the time evolution of the scalar energy dissipation rate field, in Fig. 6 we show $\log_e \nabla\zeta \cdot \nabla\zeta(\mathbf{x},t)$ in the same spatial data plane but from four temporally successive three-dimensional data volumes (see Fig. 2). Time increases in the clockwise direction beginning at the upper left. Here
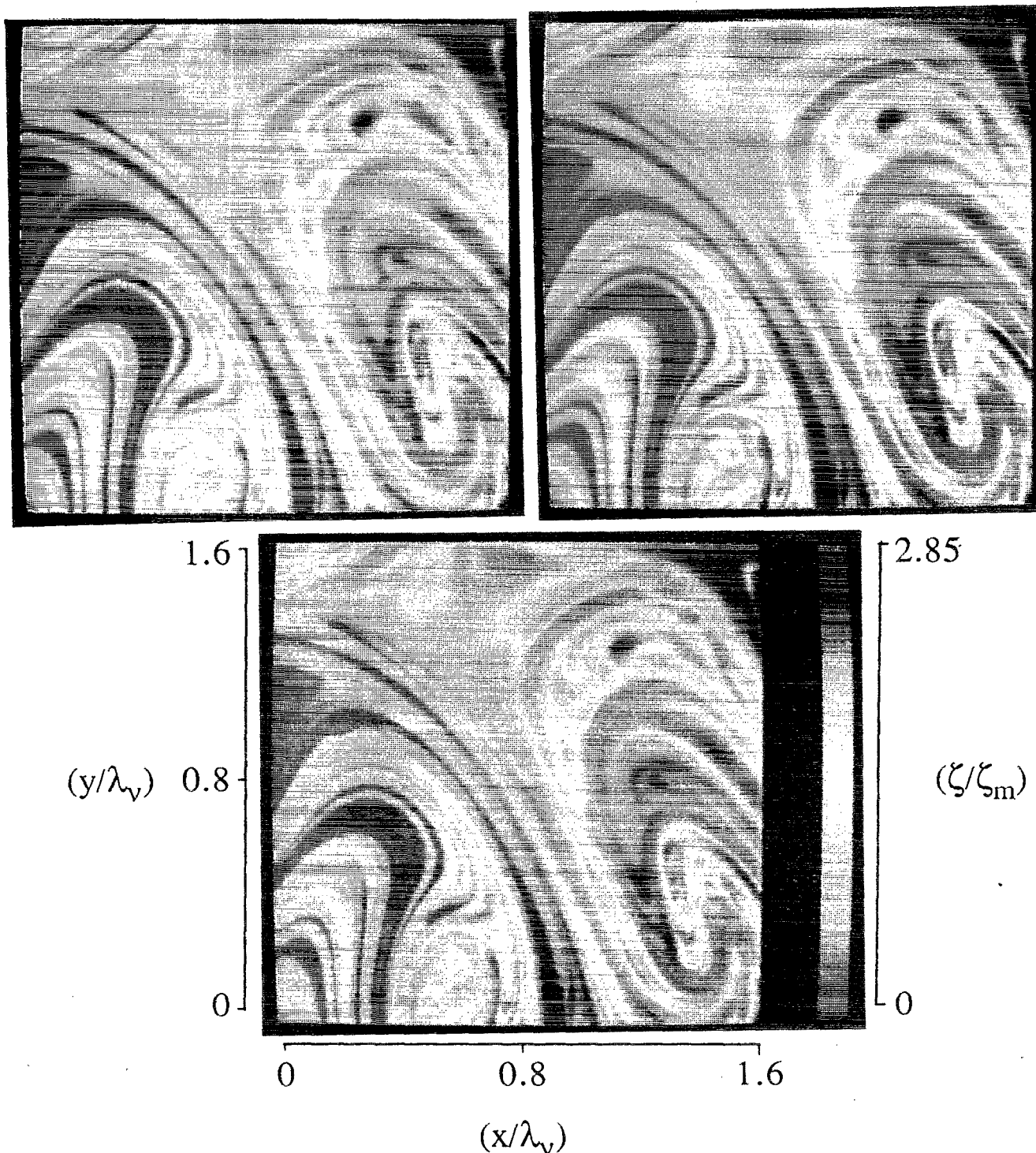
FIG. 4. The measured Sc ≫ 1 conserved scalar field $\zeta(x,t)$ in three typical successive 256×256 spatial data planes. The 256 different colors denote the local conserved scalar value at each data point. The x axis points to the right, the y axis points up, and the z axis points out of the page. The three planes are shown in order of increasing z (and therefore increasing t) in the clockwise direction, beginning at the upper left. Each data plane spans approximately $\frac{1}{17}$ of the local outer scale δ in Fig. 1, or approximately 1.6 times the local inner scale λ_ν, in both directions. The true scalar energy dissipation rate field obtained by differentiation of these data in all three directions is shown in Fig. 5.

the comparatively small change in the dissipation field between one data volume and the next, relative to the diffusion layer thickness, provides a clearer indication of the temporal resolution of the measurements.

The fine structure maps of the instantaneous scalar dissipation field in Figs. 5 and 6 clearly show that essentially all of the molecular mixing occurs in thin sheet-like layers of the type described by Burgers and Townsend for the vorticity
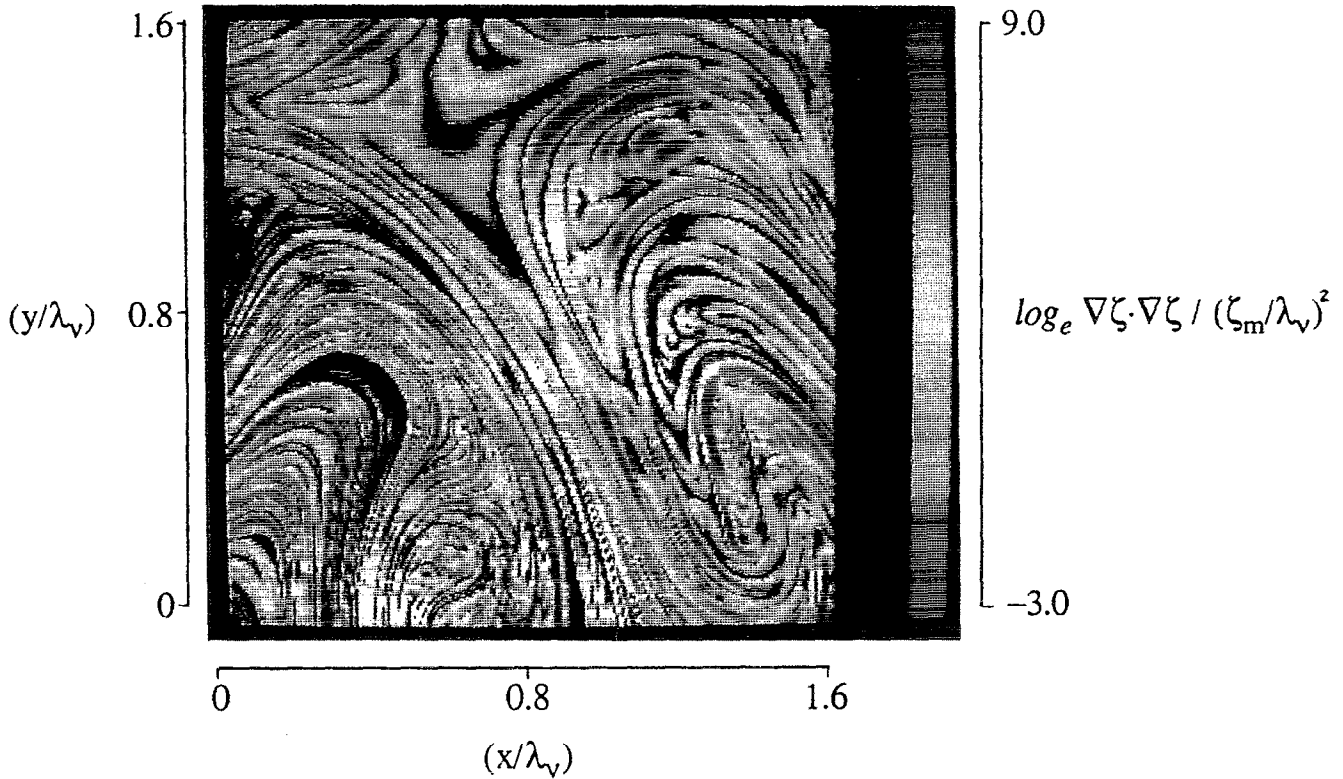
FIG. 5. The logarithm of the scalar energy dissipation rate field $\log_e \nabla\zeta\cdot\nabla\zeta(\mathbf{x},t)$ in a typical spatial data plane, obtained by direct differentiation of the conserved scalar data in the three adjacent data planes shown in Fig. 4 using linear central differences. The 256 different colors give the logarithm of the local instantaneous mixing rate in the flow. Note the fine structure of the molecular mixing process as a collection of sheet-like strained molecular diffusion layers. The time evolution of the dissipation field in this spatial data plane is shown in Fig. 6.

field. Both isolated and interacting layers can be seen. This appears to confirm the earlier conclusions in Refs. 15–17 based on lower-dimensional measurements. Especially relevant in this connection are the broad features of relatively high dissipation near the center of the upper portion of the data planes in Figs. 5 and 6. While these at first appear to not be layer-like structures, we find that most of the dissipation in these areas is due to the $(\partial\zeta/\partial z)^2$ contribution. In other words, the local scalar gradient vector is oriented largely normal to the data plane and corresponds to a layer-like structure which is cut nearly tangentially by the plane. All such layers oriented largely parallel to the data plane, as well as their contribution to the total mixing in the flow, are of course missed in lower-dimensional measurements of the dissipation. The internal structure of the molecular mixing within the layers apparent in Figs. 5 and 6 can also be examined from our measurements, and confirms the conclusions in Refs. 15–17 that strain-limited solutions of the Burgers and Townsend form give a remarkably accurate description of the true scalar energy dissipation profiles within these layers.

B. Isotropy

We first quantify the degree of anisotropy in the scalar gradient vector field captured in our four-dimensional data space by computing the probability densities for the square of each of the three components of $\nabla\zeta(\mathbf{x},t)$. In each case, the deconvolved 8-bit scalar field data is used to compute 16-bit values for the contribution of each of the gradient vector components to the dissipation, namely $\log_e (\partial\zeta/\partial x_i)^2$ using a 22-point procedure among the surrounding 26 points to compute each of the directional derivatives squared. As these calculations proceed throughout the entire data space, the histogram for each of the resulting components is constructed using 1024 bins of uniform width in linear coordinates. The resulting histograms clearly show the effects of the original 8-bit digital discretization at very low values of the dissipation. For this reason a Gaussian filter with varying width along the histogram (having a FWHM of no more than 40 bins out of the 1024 at the low end of the histogram and decreasing to no more than 10 bins out of the 1024 at the high end) is passed over each result, for which it is verified that this filtering does not affect the shape of the histogram except at the very lowest values. The filtered histogram is then renormalized to unity area and truncated at that value below which the comparison between the unfiltered and filtered results begin to show appreciable differences. All of the pdf's presented here were computed in this manner.

The resulting distributions of $\log_e (\partial\zeta/\partial x_i)^2$ are shown in Fig. 7 and summarized in Table I. Note that y points in the
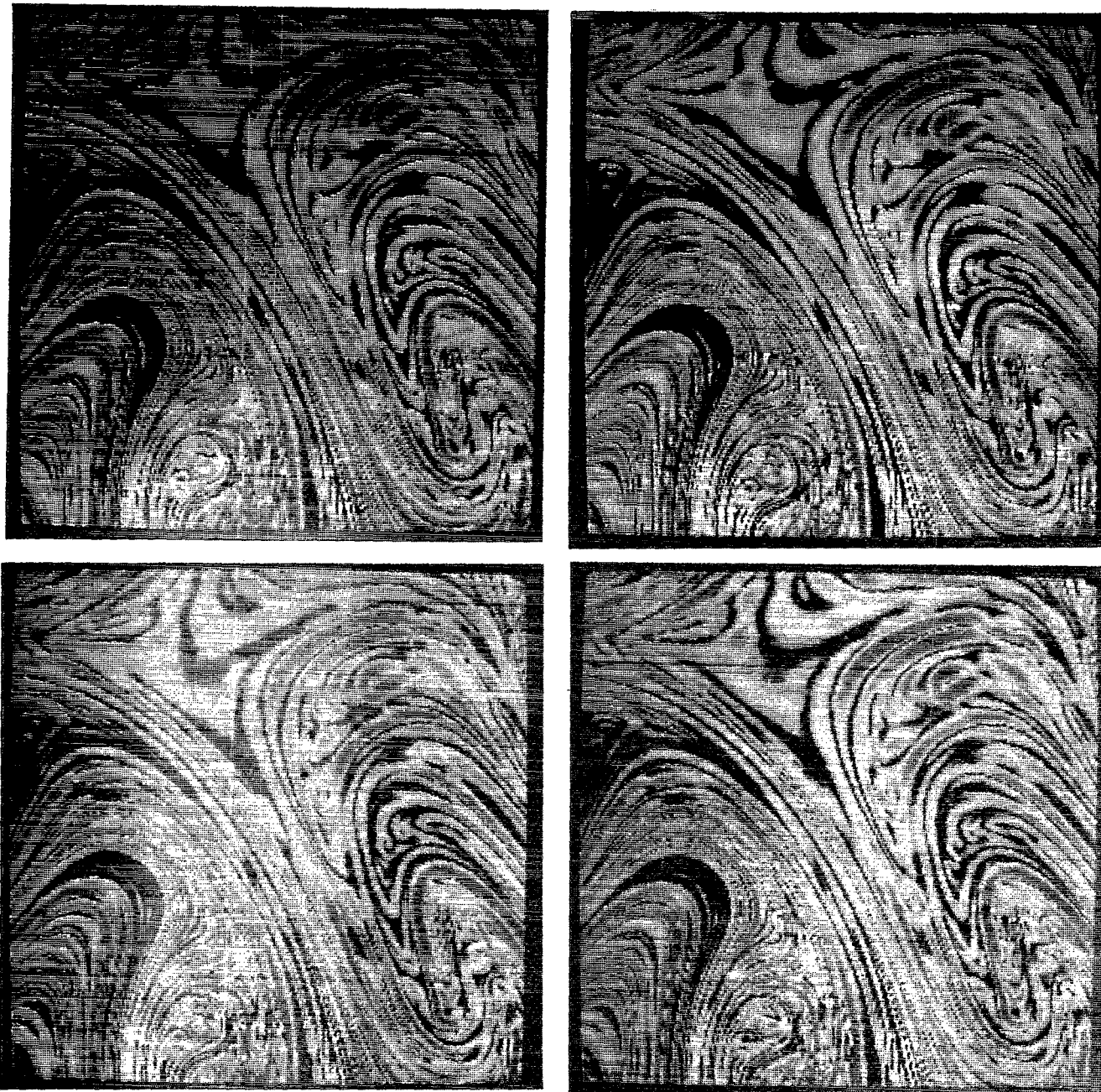
FIG. 6. The time evolution of the scalar energy dissipation rate field $\log_e \nabla\zeta\cdot\nabla\zeta(\mathbf{x},t)$ in a typical data plane from four temporally successive three-dimensional spatial data volumes (see Fig. 2). Time increases in the clockwise direction beginning at the upper left. Note that the resulting ΔT is slightly less than $\frac{1}{2}(\lambda_D/u)$. Color assignments are the same as in Fig. 5.

upstream direction, x points radially outward. If the scalar field captured were fully isotropic, then all of these distributions would be identical, and it is clear that this is not the case. In particular, the average values of $(\partial\zeta/\partial x)^2$, $(\partial\zeta/\partial y)^2$, and $(\partial\zeta/\partial z)^2$ are, respectively, in the ratio $(2.18):(1.64):(1.00)$, indicating that the gradient vector shows a tendency to point more toward the x direction than either the y or z directions. This appears consistent with the fine structure of the scalar dissipation field in Figs. 5 and 6, which show a preponderance of layers oriented somewhat

more normal to the x axis than toward the y or z axes. It appears likely that this does not represent an underlying anisotropy in the self-similar far field of turbulent jets, especially in view of the relatively small region of the flow spanned by each of the spatial data volumes (see Fig. 1). Instead, this would seem more likely to be an indication of the somewhat marginal statistical significance of the relatively short time series represented by the temporal dimension of our four-dimensional data. We examine this in greater detail below.

We can view the anisotropy suggested by Fig. 7 more

TABLE I. Statistics of the scalar gradient field $\nabla\zeta(\mathbf{x},t)$ and the associated scalar dissipation rate field $\nabla\zeta\cdot\nabla\zeta(\mathbf{x},t)$ obtained from the present measurements.

	Mean	rms
$\left(\dfrac{\partial\zeta}{\partial x}\right)^2$	193.1	390.8
$\left(\dfrac{\partial\zeta}{\partial y}\right)^2$	146.0	319.0
$\left(\dfrac{\partial\zeta}{\partial z}\right)^2$	88.7	197.0

FIG. 8. The spherical orientation angles ϑ and φ of the scalar gradient vector $\nabla\zeta(\mathbf{x},t)$ relative to the x-y-z coordinate axes in Figs. 4–6.

directly in terms of the joint probability density $\beta(\vartheta,\varphi)$ of the spherical orientation angles ϑ and φ of the scalar gradient vector $\nabla\zeta(\mathbf{x},t)$, defined in Fig. 8. The resulting joint distribution is shown in Fig. 9, and the individual probability densities $\beta(\vartheta)$ and $\beta(\varphi)$ are shown in Figs. 10(a) and 10(b), respectively. Note that, if the scalar field were fully isotropic and the gradient vector orientation were statistically independent of its magnitude, then the probability that the gradient vector in Fig. 8 will point in any given direction would be the same for all directions, giving $\beta(\vartheta,\varphi) = (1/4\pi)\sin\varphi$, while $\beta(\vartheta) = 1/2\pi$ and $\beta(\varphi) = \tfrac{1}{2}\sin\varphi$. These general features are indeed identifiable in Figs. 9 and 10. In particular, Figs. 9 and 10(a) show an at least roughly sinusoidal variation in the distribution of φ obtained from the measurements. Note that the comparatively lower probability of φ being near 0 or π is consistent with the lower values of $(\partial\zeta/\partial z)^2$ noted above. Figures 9 and 10(b) show relatively little consistent variation in the observed distribution of ϑ save for the two peaks near 0 and π, corresponding to the same tendency noted in Figs. 5–7 for the gradient vector to point more strongly in the x direction.
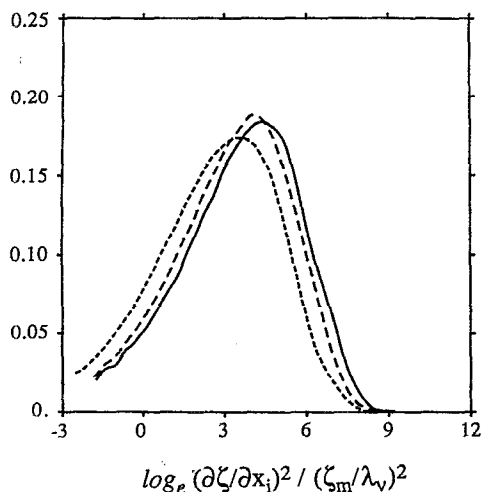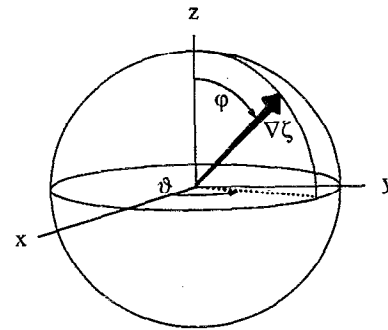
Again, the anisotropy apparent in Figs. 9 and 10 seems

likely to be more a feature of the relatively short duration over which the measurements of the scalar field were obtained than a feature of the overall scalar field itself. The relevant time scale for statistical significance within such a small region of the flow appears likely to be on the order of a few strain-limited vorticity length scale advection times (λ_ν/u). For the present data, the temporal dimension of the data space spans slightly less than $\tfrac{1}{2}(\lambda_\nu/u)$, so the fact that some anisotropy is seen here appears to be consistent with this comparison of time scales. Perhaps more important though is the observation that the results in Figs. 7–10, and also those in Fig. 11 below, approach the isotropy as closely as they do despite the comparison of time scales noted above, suggesting that the time scale required to achieve statistically isotropic scalar field data in a larger measurement of this type is indeed likely to be only a very few (λ_ν/u).

C. Mixing rate distributions

The distributions in Fig. 7 of the square of each component of the gradient vector are, in effect, one-dimensional estimates of the distribution of the true mixing rate $\nabla\zeta\cdot\nabla\zeta$. Such lower-dimensional measurements of the gradient vec-

FIG. 7. Probability densities for the logarithm of the square of each of the three vector components of $\nabla\zeta(\mathbf{x},t)$ as a check on the anisotropy of the scalar field within the four-dimensional data space; ———: $(\partial\zeta/\partial x)^2$; – – –: $(\partial\zeta/\partial y)^2$; ----: $(\partial\zeta/\partial z)^2$.
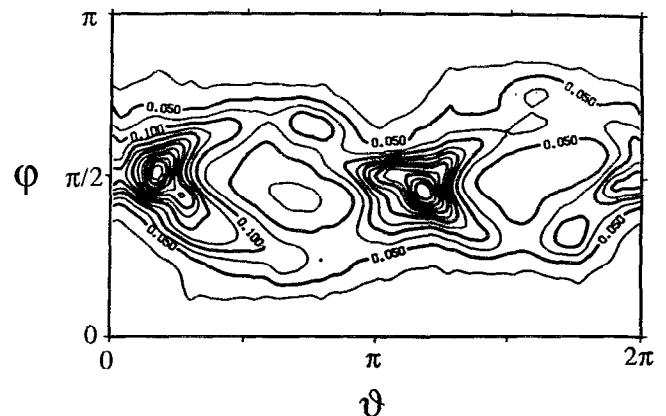

FIG. 9. The joint probability density $\beta(\vartheta,\varphi)$ of spherical orientation angles for the scalar gradient vector field $\nabla\zeta(\mathbf{x},t)$ obtained from the present measurements.
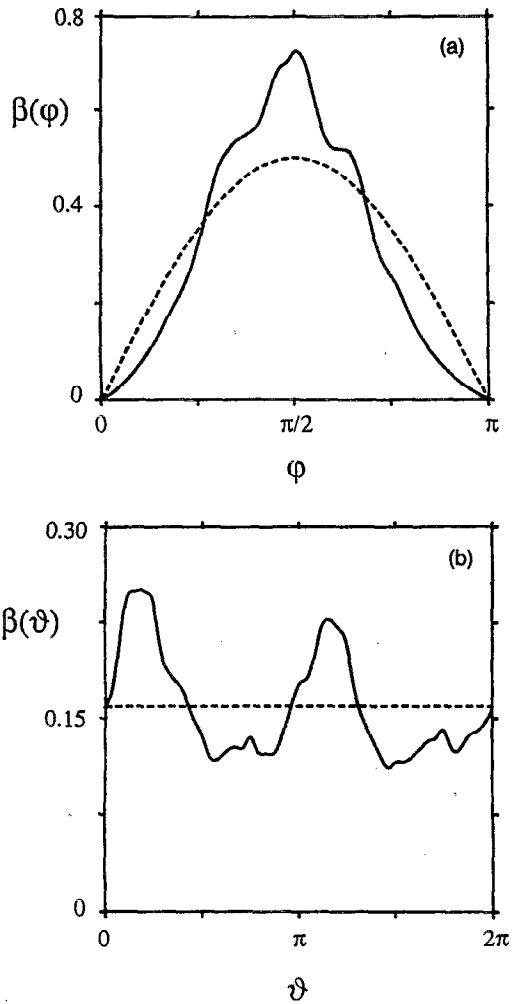
FIG. 10. The individual probability densities of spherical orientation angles for the scalar gradient vector field. (a) $\beta(\varphi)$ giving orientation relative to the z axis. (b) $\beta(\vartheta)$ giving orientation of the gradient vector projection into the x-y plane.

FIG. 11. The distribution of mixing rates obtained from one- and two-dimensional approximations of the scalar dissipation $\nabla\zeta\cdot\nabla\zeta(\mathbf{x},t)$, compared with the result obtained from all three components of the gradient field; ----: $(\partial\zeta/\partial x)^2$; ---: $(\partial\zeta/\partial x)^2 + (\partial\zeta/\partial y)^2$; ——: $(\partial\zeta/\partial x)^2 + (\partial\zeta/\partial y)^2 + (\partial\zeta/\partial z)^2$.

tor $\nabla\zeta$ are typically used to approximate the scalar dissipation, since information in all three spatial dimensions is not generally available. In Fig. 11, the mixing rate distributions that result from such one- and two-dimensional gradient approximations are compared with the result obtained from our fully three-dimensional measurement of the gradient. We note first that, for the lower-dimensional approximations, the discrete nature of the original 8-bit scalar measurements does not allow very low values of the dissipation to be accurately determined. This is especially true for the one-dimensional approximation, and thus these distributions have been truncated at the lowest discernible dissipation value. Irrespective of this effect, the one-dimensional approximation, and to a lesser degree the two-dimensional case, in principle have a long tail extending to the left and accounting for the spurious low dissipation values that would be obtained whenever the gradient vector has a comparatively large z component (see Dahm and Buch[30]). If, however, the probability distribution $\beta(\vartheta,\varphi)$ of the scalar gradient vector orientations is known, then the one- and two-dimensional scalar dissipation distributions lead directly to the three-di-
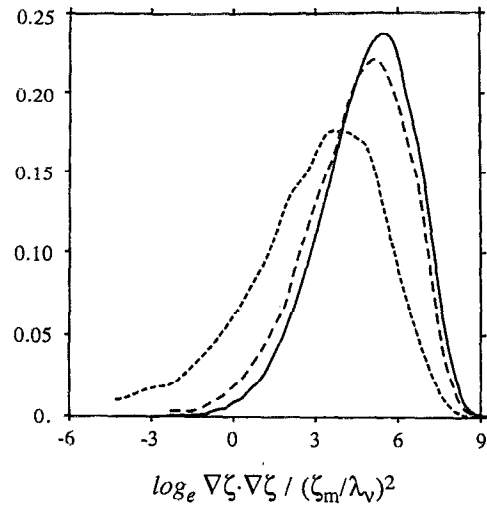
mensional distribution (see Ref. 30). Furthermore, if the scalar field were truly isotropic, then the average values of the one-, two-, and three-dimensional dissipation distributions would be in the ratio (0.33):(0.67):(1.00). The actual average values obtained from Fig. 11 are in the ratio (0.45):(0.79):(1.00), again indicating a degree of anisotropy in the comparatively short temporal extent of our measurement as noted above. Moreover, while the true scalar dissipation is often assumed to be lognormally distributed, and thus its distribution would have a Gaussian shape in Fig. 11, it is clear that the result obtained is not entirely lognormal. This too appears likely to be a manifestation of the marginal statistical significance of our four-dimensional data space.

D. Spottiness of the dissipation field

We can recognize in Figs. 5 and 6 the spatial inhomogeneity of the scalar energy dissipation field alluded to in the Introduction. This can be seen more clearly in Fig. 12, where we show the dissipation field in linear form. Note that a very small fraction of the flow is occupied by high dissipation rates, corresponding to orange and red colorings. To directly quantify this "spottiness" in the true scalar dissipation field, we show in Fig. 13 the fraction of the total dissipation that occurs in any given volume fraction of the flow, obtained from the mixing rate distributions in Fig. 11. Also shown are the results that would be obtained from lower-dimensional measurements of the scalar dissipation in Fig. 11. Notice that, in the lower-dimensional approximations of this result, manifestations of the anisotropy noted above can be seen. In particular, in a fully isotropic scalar field the one- and two-dimensional approximations should approach 0.33 and 0.67, respectively. Here the comparatively smaller z component of the scalar gradient, apparent in Figs. 5–11, renders the in-plane approximations somewhat higher than this. We also
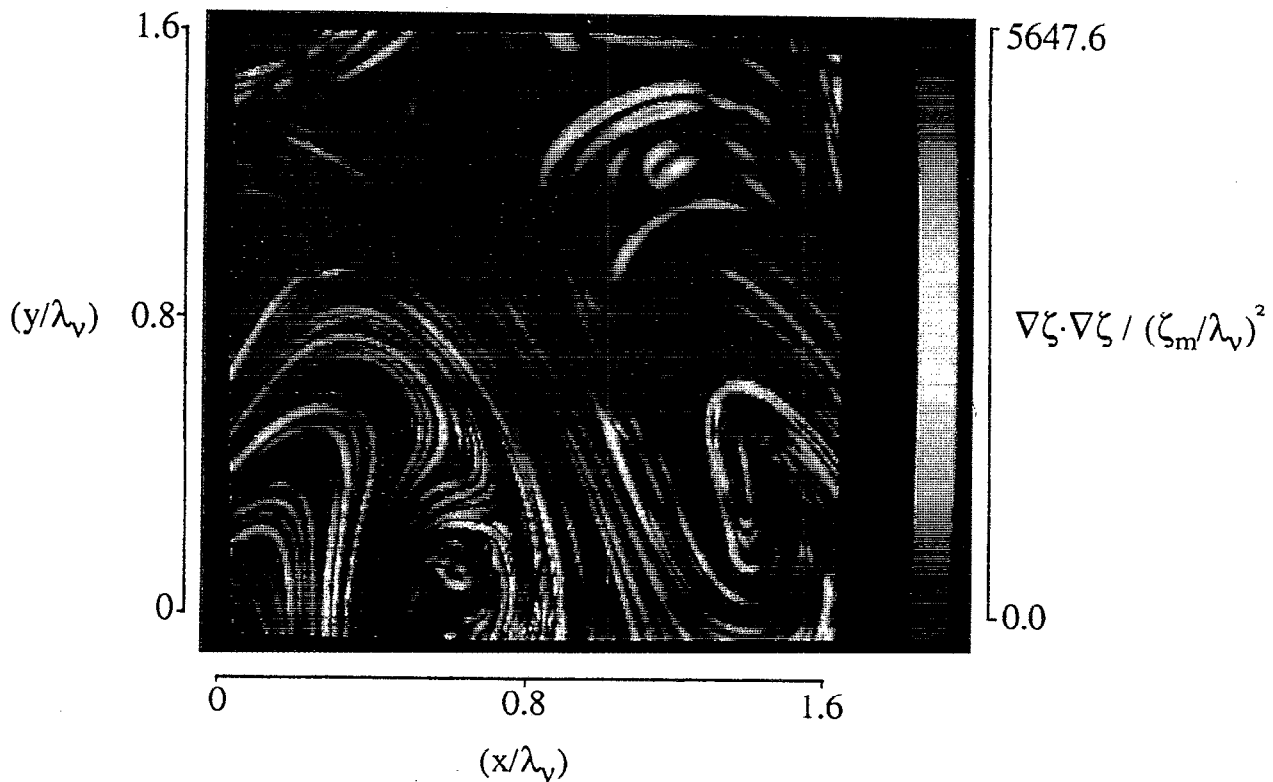
The scalar dissipation field figure with axes labeled (y/λ_ν) ranging 0 to 1.6 and (x/λ_ν) ranging 0 to 1.6, with colorbar $\nabla\zeta\cdot\nabla\zeta / (\zeta_m/\lambda_\nu)^2$ from 0.0 to 5647.6.

FIG. 12. The scalar energy dissipation rate field $\nabla\zeta\cdot\nabla\zeta(x,t)$ in the same data plane shown logarithmically in Fig. 5. Colors from blue to red denote linearly increasing dissipation rates. Note that only very little of the flow contains high dissipation rates, indicating the "spottiness" of the dissipation field.

show in Fig. 13 the curves for a lognormally distributed dissipation field, for which the result can be obtained analytically, as well as for a spatially homogeneous dissipation field, in which case the dissipation fraction is simply equal to the volume fraction.

Particularly noteworthy in Fig. 13 is the result obtained from the true dissipation that just over 1% of the total volume of the flow accounts for nearly 10% of the total dissipation, while less than 12% of the total volume achieves 50% of the total dissipation, and 45% of the volume accomplishes nearly 90% of the dissipation. This rather strikingly quantifies the fact that a very small fraction of the flow accounts for the bulk of the mixing achieved. Viewed another way, 65% of the flow accomplishes less than 10% of the total mixing. Whether the result in Fig. 13 will vary with increasing Reynolds number and from one flow to another, or whether instead the separation between the local outer scale δ and the inner scale λ_ν in these measurements is large enough to achieve Reynolds number independence and flow independence on the scale of our data volume, remains an open question. The restrictions on the Reynolds number introduced by the resolution requirements preclude, at least for the present time, comparably resolved measurements at much higher Reynolds numbers.
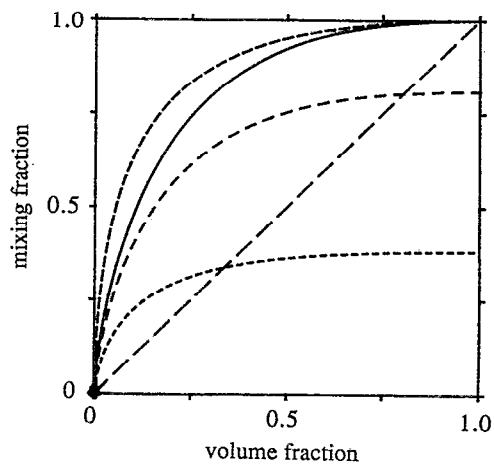

FIG. 13. The fraction of the total mixing achieved by the flow versus the fraction of the total volume within which the mixing occurs, quantifying the "spottiness" of the scalar dissipation field. Note, for example, that nearly 10% of the mixing is achieved in just 1% of the volume, 50% of the mixing is accomplished in slightly less than 12% of the volume, and 90% of the mixing occurs in just over 45% of the volume. Also shown are the results obtained from lower-dimensional approximations of the dissipation field. Present 3-D result:——— ; 2-D approximation:– – –; 1-D approximation: --- -; lognormal result: – – –; homogeneous result: — —.

1126   Phys. Fluids A, Vol. 3, No. 5, May 1991

Dahm, Southerland, and Buch   1126

IV. CONCLUDING REMARKS

The results presented here provide to our knowledge the first very highly resolved, four-dimensional measurements of the fine scale structure of conserved scalar mixing in a turbulent flow. When the results are interpreted in terms of the local inner scales of the underlying vorticity field, we believe that many features of the fine structure captured in our four-dimensional data space are to a significant degree generic to large Schmidt number mixing in all high Reynolds number turbulent flows. In particular, our fine structure maps of the instantaneous scalar dissipation field show that essentially all of the molecular mixing occurs in thin sheet-like layers of the type described by Burgers and Townsend for the vorticity field. The observation of such a layer-like fine structure is certainly reminiscent of the lamellar micro-structure seen in recent experiments on mixing in low Reynolds number chaotic flows (e.g., Refs. 8–10), and suggests a degree of universality in the fine structure that extends across the boundaries of the Reynolds number regimes traditionally associated with such comparatively simple chaotic flows and the turbulent flows investigated here. Of course, our present measurements give no direct information about the kinematical foundation for these layers, yet their presence is suggestive of a significant correlation between the scalar gradient vector direction and the most compressive principle strain rate axis (see, for example, Refs. 4 and 31). Both isolated and interacting layers can be seen. Various tests of the isotropy of this fine structure within our four-dimensional data space suggest that a temporal extent of just a few strain-limited vorticity length scale advection times (λ_ν/u) appears to be sufficient in a larger measurement of this type to produce statistically isotropic scalar field data. Perhaps most striking in our results is the quantification in Fig. 13 of the "spottiness" in the fine structure of the scalar energy dissipation field, which directly shows that a remarkably small fraction of the flow accounts for a surprisingly large fraction of the mixing. Conversely, a large fraction of the flow participates almost negligibly in the mixing process. To what extent the quantitative features in Fig. 13 are an unavoidable and universal characteristic of the sheet-like fine structure of $\mathrm{Sc} \gg 1$ mixing in all high Reynolds number turbulent flows, or whether instead certain flows can, in the sense of Fig. 13, be made more efficient "mixers" than others, would certainly appear to be an important question.

ACKNOWLEDGMENTS

[1] A. N. Kolmogorov, C. R. Acad. Sci. URSS **30**, 301 (1941).
[2] G. K. Batchelor, J. Fluid Mech. **5**, 11 (1959).
[3] J. M. Burgers, Adv. Appl. Mech. **1**, 171 (1948).
[4] A. A. Townsend, Proc. R. Soc. London Ser. A **208**, 534 (1951).
[5] F. S. Sherman, *Viscous Flow* (McGraw-Hill, New York, 1990).
[6] G. K. Batchelor, *An Introduction to Fluid Dynamics* (Cambridge U.P., Cambridge, 1967).
[7] G. F. Carrier, F. E. Fendell, and F. E. Marble, SIAM J. Appl. Math. **28**, 463 (1975).
[8] J. M. Ottino, Sci. Am., January, 56 (1989).
[9] J. M. Ottino, Phys. Fluids A. **3**, 1417 (1991).
[10] J. M. Ottino, C. W. Leong, H. Rising, and P. D. Swanson, Nature **333**, 419 (1988).
[11] J. M. Ottino, J. Fluid Mech. **114**, 83 (1982).
[12] J. M. Ottino, *The Kinematics of Mixing: Stretching, Chaos and Transport* (Cambridge U.P., New York, 1989).
[13] J. M. Ottino, Annu. Rev. Fluid Mech. **22**, 207 (1990).
[14] J. R. Bourne, submitted to Phys. Fluids A. (1990).
[15] W. J. A. Dahm and K. A. Buch, *Turbulent Shear Flows* (Springer-Verlag, Berlin, 1990), Vol. 7.
[16] W. J. A. Dahm and K. A. Buch, submitted to J. Fluid Mech.
[17] W. J. A. Dahm and K. A. Buch, submitted to J. Fluid Mech.
[18] W. J. A. Dahm, K. B. Southerland, and K. A. Buch, *Proceedings of the 5th International Symposium on Applications of Laser Techniques to Fluid Mechanics*, (Instituto Superior Technico, Lisbon, 1990).
[19] R. K. Hanson, *Proceedings of the 21st Symposium (International) on Combustion* (The Combustion Institute, Pittsburgh, 1986), p. 1677
[20] B. Yip and M. B. Long, Opt. Lett. **11**, 64 (1986).
[21] D. C. Fourguette and M. B. Long, Opt. Lett. **9**, 270 (1983).
[22] B. Yip, M. B. Long, and D. C. Fourguette, Appl. Opt. **25**, 3919 (1986).
[23] B. Yip, J. K. Lam, M. Winter, and M. B. Long, Science **235**, 1209 (1987).
[24] B. Yip, R. L. Schmitt, and M. B. Long, Opt. Lett. **13**, 96 (1988).
[25] R. P. Prasad and K. R. Sreenivasan, J. Fluid Mech. **216**, 1, 1990.
[26] T. K. Sherwood, R. L. Pigford, and C. R. Wilke, *Mass Transfer* (McGraw-Hill, New York, 1975).
[27] S. Biringen, VKI Tech. Note 110, 1975.
[28] F. E. Marble, *Recent Advances in Aerospace Sciences*, edited by C. Casci (Plenum, New York, 1985), p. 395.
[29] D. R. Dowling, Ph.D. thesis, California Institute of Technology, Pasadena, 1987.
[30] W. J. A. Dahm and K. A. Buch, Phys. Fluids A **1**, 1290 (1989).
[31] Wm. T. Ashurst, A. R. Kerstein, R. M. Kerr, and C. H. Gibson, Phys. Fluids **30**, 2343 (1987).